Development of an Open Rotor Propulsion System Model and Power Management Strategy

Robert A. Clark *, Christian Perron †, Jimmy Tai ‡, Benjamin Airdo §, and Dimitri N. Mavris ¶
Georgia Institute of Technology, Atlanta, Georgia, 30332

The development of an open rotor propulsion system architecture model and fuel burn-minimizing power management strategy is investigated. The open rotor architecture consists of a single-rotor open rotor (SROR) connected to the low speed shaft of a traditional turbojet engine in a puller configuration. The proposed architecture is modeled in the Numerical Propulsion System Simulation (NPSS) tool, and performance is evaluated across a complete flight envelope typical for a narrow body commercial airliner. Rotor performance maps are generated using a custom blade element momentum theory (BEMT) code, while compressor performance maps are created using CMPGEN. The performance of the overall propulsion system is detailed in the context of a notional 150 passenger aircraft mission, and a method for scheduling rotor power across the flight envelope is developed in order to minimize aircraft mission fuel burn. It is demonstrated that the power absorbed by the rotor can be optimized by scheduling rotor blade pitch angle versus fan speed. A power management technique using the optimal blade pitch angle at only six points in the flight envelope was shown to provide significant computational benefits without sacrificing any fuel burn when compared to a method using a schedule generated from data across the complete flight envelope.

Nomenclature

A	=	Rotor area
C_P	=	Power coefficient
C_T	=	Thrust coefficient
D	=	Rotor diameter
J	=	Advance ratio
n	=	Rotor rotational speed [rev/s]
$N1$	=	Low-speed shaft
$N2$	=	High-speed shaft
N_c	=	Corrected speed [rpm]
$NcPct$	=	Corrected speed as a percentage
P	=	Power
r	=	Radial position
R	=	Rotor radius
R_{hub}	=	Rotor hub radius
$T41$	=	High Pressure Turbine Inlet Temperature
u_a, u_t	=	Externally induced velocity
v_a, v_t	=	Self-induced velocity
V_∞	=	Free-stream velocity
V_{eff}	=	Effective velocity
W	=	Flow rate [lbm/s]
x	=	Axial position
α	=	Angle of attack

*NDSEG Fellow, Aerospace Systems Design Laboratory, AIAA Student Member.
†Research Engineer, Aerospace Systems Design Laboratory.
‡Senior Research Engineer, Aerospace Systems Design Laboratory, AIAA Associate Member.
§Undergraduate Student, Aerospace Systems Design Laboratory.
¶S.P. Langley Distinguished Regents Professor, Aerospace Systems Design Laboratory, AIAA Fellow.

β = blade section pitch angle
η = Overall efficiency
η_p = Propulsive efficiency
η_{prop} = Rotor efficiency
η_t = Thermal efficiency
ρ = Density
Ω = Rotor rotational speed [rad/s]
ϕ = Effective flow angle

I. Introduction

Rising fuel prices and an ever-increasing focus on aviation emissions have led to continual improvements over time by aircraft engine manufacturers with respect to fuel burn and propulsion system efficiency. Overall propulsion system efficiency can be thought of as the product of two types of efficiency: the thermal efficiency η_t and propulsive efficiency η_p. Advancements in metallurgy and composite materials have expanded the operational temperature range of air-breathing propulsion systems in an effort to improve thermal efficiency, while also enabling lighter propulsion systems. Furthermore, fan diameters have continued to increase in an attempt to improve propulsive efficiency. However, while propulsion systems today are more efficient than ever, they still primarily fall under the same architecture, i.e., high bypass ratio turbofans. The introduction of a gearbox between the low-pressure turbine (LPT) and the fan, such as in the Pratt & Whitney PW1000G family of engines, is a small departure from the typical propulsion system architecture that enables larger fan diameters and higher propulsive efficiency, but even still the architecture remains largely the same.

However, step-changes in efficiency can be achieved by departing from the typical high bypass ratio turbofan concept and adopting new propulsion system architectures. One such potential architecture is the unducted fan (UDF), also known as a propfan or an open rotor architecture. In a typical (ducted) turbofan engine, the first compression element, known as the fan, has a shroud (the fan duct) around the fan blades, and the assembly is contained within the overall engine nacelle. In this conventional design, the nacelle helps to attenuate noise produced by the fan. An unducted fan, however, has no such shroud around the rotating fan blades. This allows for much larger diameters, but comes at the cost of higher noise. Fig. 1 shows a notional trend of propulsive efficiency versus fan pressure ratio, with open rotor designs achieving significantly higher propulsive efficiencies than typical ducted turbofans [1, 2].

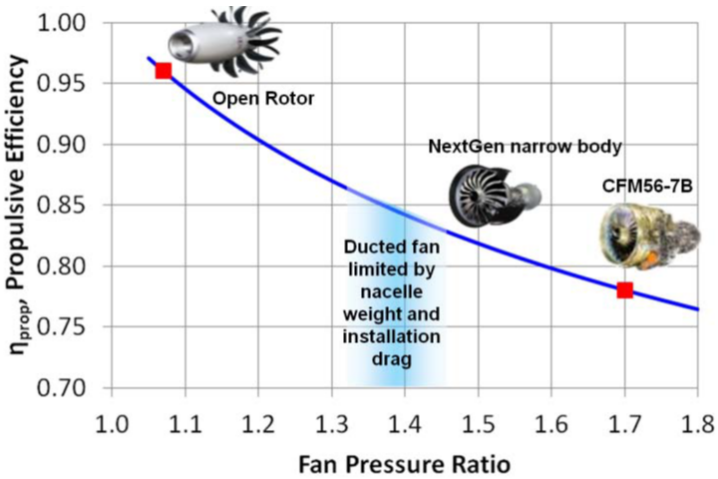

Fig. 1 Propulsive Efficiency versus Fan Pressure Ratio (reproduced from [1])

Open rotor architectures come in two primary variations: puller-type configurations, where the rotor is forward of the propulsion system core, and pusher-type configurations, where the rotor is aft of the propulsion system core [3]. To further increase propulsive efficiency, the main rotor is often paired with an aft counter-rotating rotor that attenuates the swirl of the former. A similar effect can be achieved using instead static swirl recovery vanes (SRV) [4, 5], which are less effective than a counter-rotating rotor, yet are mechanically simpler. The open rotor architecture has been under investigation for several decades, with particular emphasis in the 1980s when the General Electric GE36 and Pratt &

Fig. 2 CFM RISE Conceptual Drawing [11]

Whitney / Allison 578-DX, both pusher configurations, underwent development far enough to achieve successful flight test demonstrations. The GE36 involved two counter-rotating rotors connected to a free-power turbine (FPT), and was based on the core of the F404 engine [6, 7]. Both GE and Pratt & Whitney expected these open rotor engines to be certified by 1992 [8]. However, these programs, initially driven by skyrocketing fuel prices, became less attractive when fuel prices dropped, and development was halted. In recent years, however, interest has re-emerged in open rotor architectures, with Safran performing open rotor demonstrator tests in 2017 [9, 10], and CFM announcing the RISE program (Revolutionary Innovation for Sustainable Engines) in 2021 [11]. A conceptual drawing of the CFM RISE engine can be seen in Fig. 2. Notably, the CFM RISE concept shows a departure from previous architectures by favoring the use of static SRVs over a counter-rotating rotor.

To that effect, the current work presents the development of an open rotor propulsion system architecture model and the investigation of a fuel burn-minimizing power management strategy. The remainder of this paper presents the selected open rotor architecture, the methodology used for the rotor aerodynamic modeling, and the strategy for the system performance modeling. This is followed by a description of the proposed power management strategy. Finally, results are presented showing the benefits of the proposed strategy and assessing the merits of the open rotor architecture.

II. GT-SROR Architecture Selection

The Georgia Tech Single-Rotor Open Rotor (GT-SROR) is intended to closely represent the CFM RISE engine, as seen in Fig. 2, which is a puller-type open rotor engine with a single row of rotating rotor blades followed by a stationary row of SRV. The turbomachinery core is essentially a turbojet configuration, with a high-pressure compressor (HPC) connected to a high-pressure turbine (HPT) on the high-speed shaft (N2), and a low pressure compressor (LPC) connected to a low-pressure turbine (LPT) on the low-speed shaft (N1).

In one potential architecture, the rotor is connected to the front of the low-speed shaft through a reduction gearbox, while a different architecture has the rotor connected to a free-power turbine (FPT) via a reduction gearbox on a separate third shaft. Both of these potential configurations are enumerated by Zatorski et al. in United States Patent 10,704,410 [12]. At the time of writing, public-domain literature released by CFM does not indicate whether or not the rotor has its own turbine. Therefore, for the work described in this paper, modeling is focused on the first architecture, where the rotor is connected to the N1 shaft with the LPC and is powered by the LPT.

III. Rotor Performance Mapping

Performance estimates for the open rotor are obtained through the development of a custom blade element momentum theory (BEMT) Python code, which is able to generate rotor performance maps suitable for use across the flight envelope. The performance maps are used to tabulate rotor efficiency η_{prop}, thrust coefficient C_T, and pitch angle β versus flight Mach number, power coefficient C_P, and advance ratio J. Definitions for these quantities are given as

$$C_T = \frac{T}{\rho n^2 D^4} \qquad J = \frac{V_\infty}{nD} \tag{1}$$
$$C_P = \frac{P}{\rho n^3 D^5} \qquad \eta_{\text{prop}} = J\frac{C_T}{C_P}$$

where p is the air density, n is the rotor rotational speed in rev/sec, D is the rotor diameter, and V_∞ is the free-stream velocity.

A. BEMT Formulation

Considering a rotor and the stream tube that traverses it, the BEMT method discretizes this problem radially in terms of blade elements and corresponding stream tube annuli. Subsequently, the method seeks a flow solution that balances the sectional forces produced by the blade elements and the changes in momentum experienced by the stream tube annuli [13, 14]. Note that this is a two-way coupling as the blades induce axial and rotational momentum to the stream tube, which in turn affects the relative flow velocity and angle perceived by the blades. Fig. 3 shows the velocity triangle of a rotor blade section. In this figure, V_{eff} is the effective velocity vector of the blade section. The axial component of V_{eff} depends on the free-stream velocity V_∞, the self-induced axial velocity v_a, and the externally induced axial velocity u_a. Specifically, v_a refers to the velocity induced by the blade section onto itself, while u_a is the velocity induced by another rotor such as in a counter-rotating configuration. Similarly, the tangential component of V_{eff} depends on the rotor angular velocity Ωr, the self-induced tangential velocity v_t, and the externally induced tangential velocity u_t.

The developed BEMT Python code finds the solution to the blade velocity triangle of Fig. 3 using a circulation-based formulation similar to the QPROP code from Drela [15]. This is summarized by the following residual equation

$$R = \Gamma - \frac{1}{2} V_{\text{eff}}\, c\, C_l \tag{2}$$

where Γ is the section circulation, c is the section chord, and C_l is the section lift coefficient. The above equation is repeated for each blade element and then is combined into a system of non-linear equations. In the current work, this system is solved using a hybrid Powell method provided by the SciPy package [16]. Note that the circulation computed in Eq. (2) considers the effect of tip losses using the established Prandtl correction factor [17]. The C_l value is obtained from 2D airfoil data and depends on the blade angle of attack α, which is the difference between the local pitch angle β and the effective flow angle ϕ (see Fig. 3). The C_l value is also affected by the effective Reynolds and Mach number which can be computed using V_{eff} and the ambient air properties. Due to the high effective Mach number the blades are expected to operate at, a swept blade geometry is considered. Similar to a swept wing, the local Mach number is corrected by a factor $\cos(\Lambda)$ where Λ is the local sweep angle of the blade. Once the solution to Eq. (2) is found, the forces on all blade elements are integrated into a thrust and power value.

The prediction capability of the developed BEMT code has been verified using wind tunnel data of the SR-3 high-speed propeller [18, 19]. Fig. 4 shows a comparison of the experimental and the predicted η_{prop} for a few operating conditions. The markers show the experimental results for a fixed blade pitch angle β_{exp}, and the solid lines represent the BEMT predictions. Note that the blade pitch of the BEMT model is adjusted to match the C_T of the experimental data to compare the rotor efficiency for the same thrust level. Overall, the BEMT results match reasonably well with the experimental data. A higher discrepancy between the numerical and experimental η_{prop} is generally observed at higher free-stream Mach number M_∞. This is likely caused by the increased presence of non-linear physics, such as shock waves and flow separation, that a simple BEMT model cannot adequately capture. Nonetheless, this level of error is acceptable for conceptual design, especially when considering these results can be obtained in the order of seconds.

B. Rotor and SRV Interaction

As depicted in Fig. 2, the open rotor configuration considered uses swirl-recovery vanes. The purpose of the SRV is to convert some of the lost kinetic energy from the rotor wake into additional thrust and increased efficiency. In a way,

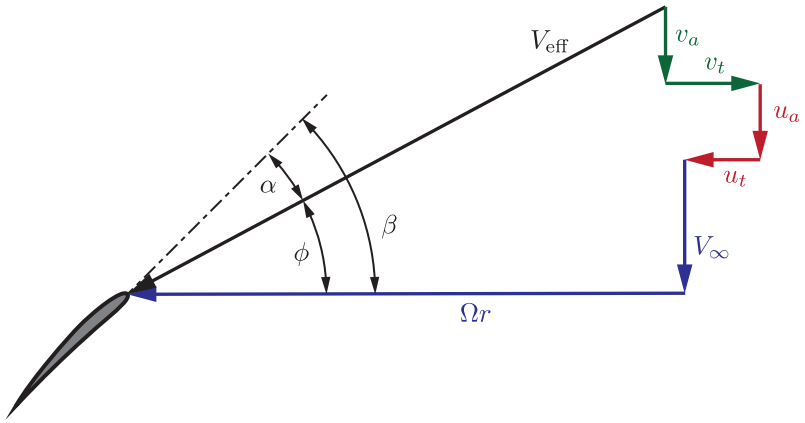

Fig. 3 Velocity triangle for a rotor blade in the BEMT model.

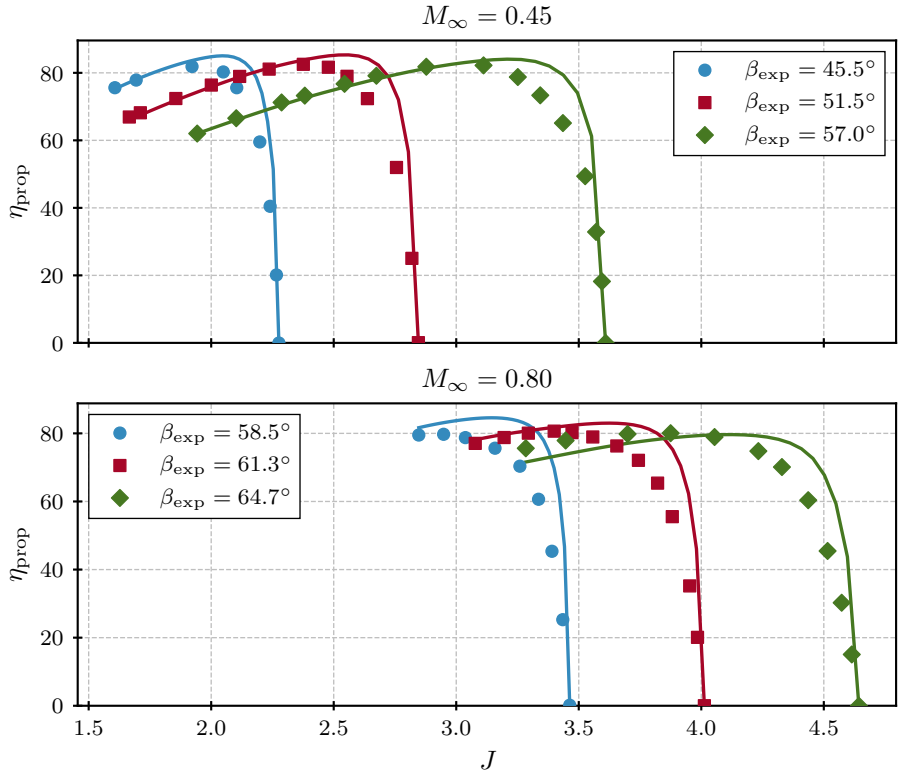

Fig. 4 Verification of the BEMT model using the SR-3 propeller experimental results [18].

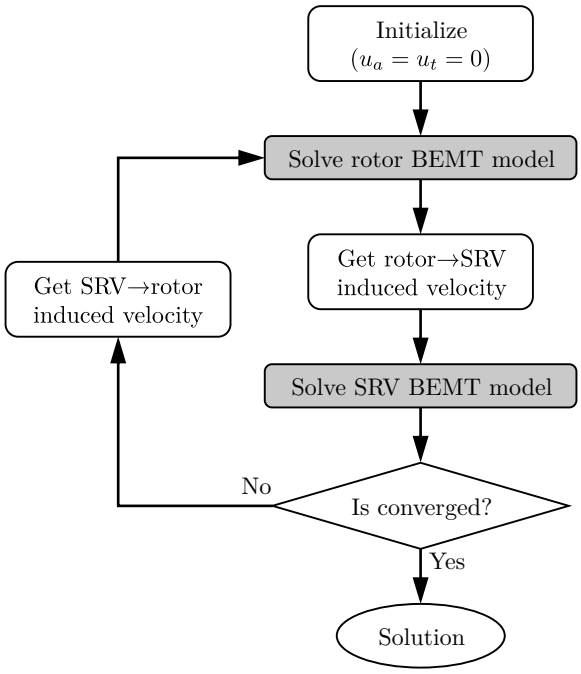

Fig. 5 Flowchart of the coupling between the rotor and SRV aerodynamics.

this configuration is similar to a counter-rotating open rotor such as the GE36, but with a non-rotating aft rotor. For this reason, the performance of the SRV can still be modeled using BEMT and by setting their rotational speed to zero (i.e., $\Omega r = 0$). While the rotor wake has a downstream effect on the SRV, the latter also has an upstream impact on the rotor performance, although to a lesser extent. This implies that the aerodynamics of the rotor and the SRV are coupled and must be solved together.

In this work, the rotor and SRV interaction is solved using a sequential approach as illustrated in Fig. 5. Both the rotor and the SRV are analyzed with individual BEMT models, and the connection between the two is captured in terms of the externally induced velocities u_a and u_t (see Fig. 3). The process begins by solving the BEMT model of the rotor without any influence from the SRV. From the obtained solution, the rotor wake velocities are used to approximate the velocities induced by the rotor onto the SRV. Then, keeping the externally induced velocities fixed, the SRV solution is obtained using its BEMT model. The velocities induced by the SRV onto the rotor are approximated, the rotor BEMT model is updated with these externally induced velocities, a new rotor solution is obtained, and the process is repeated until some convergence criterion is attained. After the convergence, the forces on both the rotor and the SRV are combined into an overall thrust and power result.

As a consequence of generating thrust, the air velocity moving through the rotor area is accelerated. Therefore, the stream tube around the rotor contracts as it progresses downstream to satisfy the conservation of mass. This phenomenon must be taken into account when considering the rotor-SRV interaction as it affects the remote influence that the rotor and SRV have on the flow field. To approximate the effect of the stream tube contraction, one can represent the rotor as an ideal actuator disk [20, 21]. With this model, the variation of the streamtube area A_x at a distance x downstream is given by

$$\frac{A_x}{A} = \frac{V_\infty + \bar{v}_a}{V_\infty + \bar{v}_{a,x}} \tag{3}$$

with

$$\bar{v}_a = \frac{1}{2}\left(-V_\infty + \sqrt{V_\infty^2 + \frac{2T}{\rho A}}\right) \tag{4}$$

$$\bar{v}_{a,x} = \bar{v}_a\left(1 + \frac{x}{R}\sqrt{1 + \frac{x^2}{R^2}}\right) \tag{5}$$

Table 1 Geometric design parameters of the GT-SROR.

Parameter	Rotor	SRV
Num. of Blades	12	10
D	12 ft	11.16 ft
D_{hub}	3 ft	3 ft
Axial Spacing	3.6 ft	

where A is the rotor area, $\bar{v}_a$ is the axial velocity induced by the actuator disk at $x = 0$, and $\bar{v}_{a,x}$ is the axial velocity induced at a distance x. Note that far upstream and downstream, Eq. (5) tends to $\bar{v}_{a,x} = 0$ and $\bar{v}_{a,x} = 2\bar{v}_a$ respectively, which is consistent with the momentum theory.

Using the model of Eq. (3), the u_a velocity profile of the SRV corresponds to the v_a velocity distribution of the rotor corrected for the stream tube contraction. These corrections include a radial redistribution of the velocity profile for the smaller area, and a scaling of the velocity magnitude to satisfy the conservation of mass of each BEMT annulus. This is represented by the following

$$R_x = \sqrt{R_{\text{hub}}^2 + A_x/\pi} \tag{6}$$

$$r_x = (r - R_{\text{hub}})\frac{R_x - R_{\text{hub}}}{R - R_{\text{hub}}} + R_{\text{hub}} \tag{7}$$

$$u_a(r_x) = \frac{A_x}{A}\, v_a(r) \tag{8}$$

where R_{hub} is the rotor hub radius, R_x is the radius of the contracted stream tube, and r_x is the corrected coordinates of the velocity distribution induced by the rotor onto the SRV. Note that in Eq. (7), a constant R_{hub} from the rotor to the SRV is assumed for simplicity. As for the tangential velocity u_t, a similar scaling is performed to keep the circulation of each BEMT annulus constant such that

$$u_t(r_x) = \frac{r_x}{r}\, v_t(r) \tag{9}$$

The influence of the SRV onto the rotor is approximated in a similar manner using Eq. (7) and (8). However, for a counter-rotating propeller, the swirl induced by the aft rotor onto the front rotor is often neglected as it is orders of magnitude smaller than the axial induced velocity [22–24]. As such, the SRV is assumed to induce no swirl upstream of it, i.e., $u_t = 0$ for $x < 0$.

C. Rotor Design and Map Generation

The open rotor design used in this study, the GT-SROR, is a visual approximation of the CRM RISE concept (see Fig. 2). Some of the main features of the considered geometry are listed in Table 1. The axial spacing listed in Table 1 refers to the axial distance between the rotor and the SRV. Note that the SRV diameter is 7% smaller than the rotor to ensure that the SRV is fully inside the rotor wake during the cruise conditions. The blade sweep of both the rotor and the SRV is selected such that the effective Mach number at cruise is 0.7 and 0.75 at the root and tip respectively. The sweep goes from a forward angle at the root to a backward angle at the tip with an inflection point at roughly 55% of the blade length, thus giving the blades a *scimitar* shape. Fig. 6 provides a visualization of the resulting rotor and SRV planforms. The airfoil stack used for both the rotor and the SRV is the same as the SR-3 propeller [18], which is a mixture of NACA 16-series and 65-series. The rotor and SRV local β angles are finally obtained by optimizing η_{prop} for a cruise power loading $P/D^2 = 40$ HP/ft^2 and a cruise rotor tip-speed $\Omega R = 800$ ft/sec, using the developed BEMT code.

From the defined open rotor geometry, a performance map is generated by using the BEMT code to compute C_T and η_{prop} for a wide range of C_P and M_∞ from 0 to 0.85. Note that the effect of altitude is neglected for the map generation as its impact on the non-dimensional performance metrics is small. At each C_P and M_∞ combination, the rotor and SRV global pitch angles β_{ref} are optimized to provide the maximum η_{prop}. In this work, β_{ref} is defined as the local β angle measured at 75% of the blade radius. Once the data is generated, it is tabulated in a format that can be easily used by the engine model (see Sct. IV). Fig. 7 shows an example of the open rotor performance obtained under the cruise conditions. In this figure, the circle marker represents the design point used for the geometry optimization, while the black and red isolines represent the rotor and SRV β_{ref} angles.

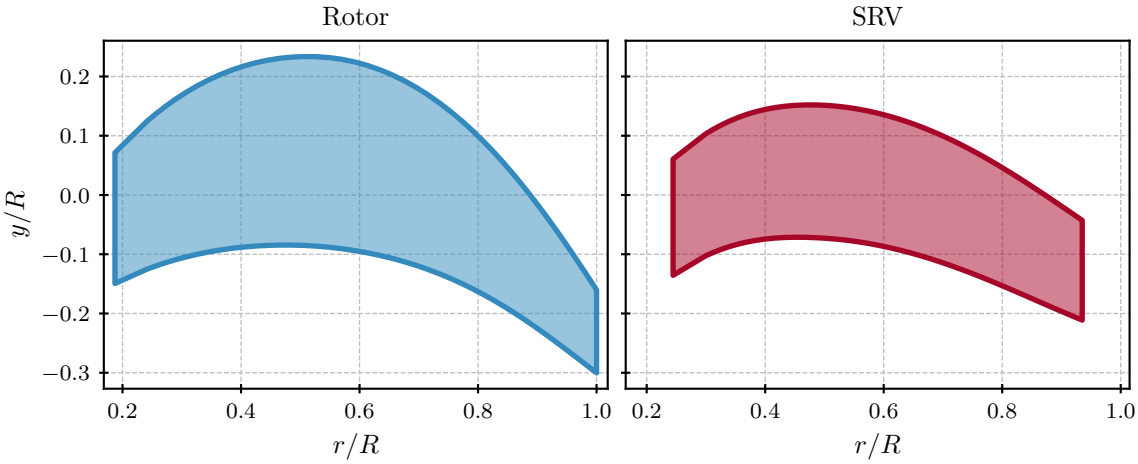

Fig. 6 Rotor and SRV blade planform of the GT-SROR.

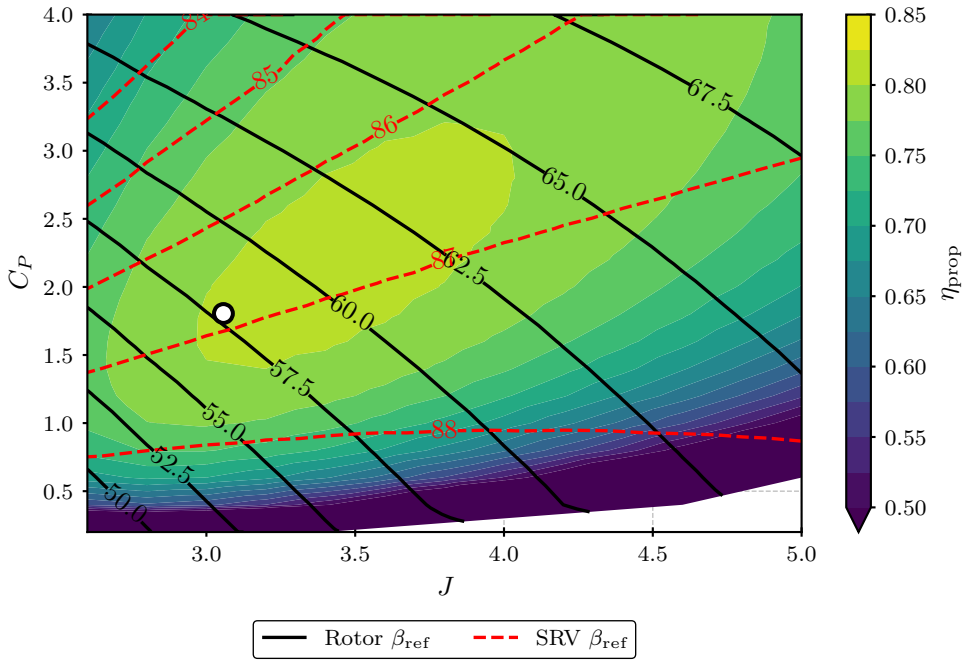

Fig. 7 Performance of the GT-SROR at $M_\infty = 0.8$ and an altitude of 35,000 ft. The circle marker represent the design point used to optimize the geometry.

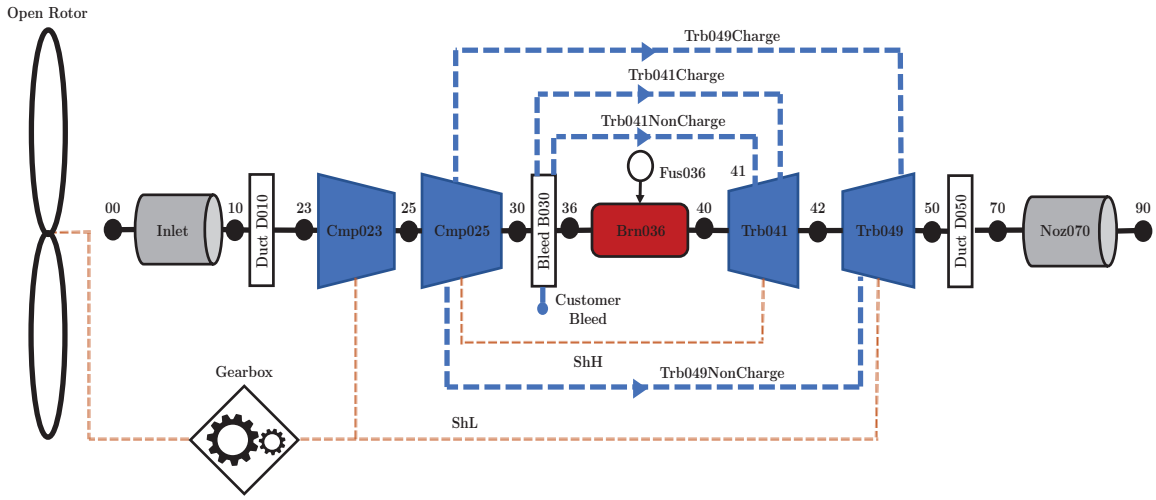

Fig. 8 Block diagram representation of the GT-SROR.

IV. SROR Propulsion System Performance Modeling

The GT-SROR architecture is modeled using NASA's Numerical Propulsion Simulation (NPSS) tool. NPSS is the industry gold-standard tool for thermodynamic modeling of propulsion systems, and while the details of NPSS are beyond the scope of this paper, Jones provides a comprehensive introduction to the methods used to build thermodynamic engine cycle models in NPSS [25]. Furthermore, an implementation of the multiple design point (MDP) method described by Schutte et al. [26–28] is utilized to ensure that the propulsion system would be able to meet design requirements at multiple different operating conditions.

Fig. 8 shows a block diagram representation of the GT-SROR NPSS model with all of the components named using station number designations as recommended by Aerospace Standard AS755F [29]. The model consists of the open rotor and low-pressure compressor (Cmp023) connected through the low-speed shaft (ShL or N1) to the low-pressure turbine (Trb049). The high-pressure compressor (Cmp025) is connected through the high-speed shaft (ShH or N2) to the high-pressure turbine (Trb041). Interstage bleed air is taken from Cmp025 for Trb049 cooling, while compressor discharge plane (CDP) air is bled at station B030 to provide Trb041 cooling. Station B030 also supplies any required customer bleed air (i.e., for other aircraft subsystems). Note that this configuration is different from prior open rotor models that were modeled after the GE36, which had pusher-type rotors connected to a counter-rotating FPT on a separate shaft [30, 31].

Performance of both the LPC and HPC is modeled using compressor maps generated with CMPGEN, a tool originally developed for NASA by GE to model compressor performance [32]. CMPGEN produces *stacked* tables that contain compressor efficiency, corrected mass flow, and pressure ratio versus compressor corrected speed (Nc) as a percentage (NcPct) and an arbitrary *Rline* map position. Jones provides additional detail on compressor maps [25]. Rotor performance is modeled using similar stacked maps that contain rotor efficiency η_{prop} and blade pitch angle β versus M_∞, J, and C_P, as described in Sct. III. For static operating conditions when $J = 0$, the rotor thrust coefficient C_T is tabulated versus the power coefficient C_P.

As noted previously, the multiple design point (MDP) method is used in the development of the GT-SROR model. The gist of the MDP method is that a cycle can be sized at one operating condition referred to as the aerodynamic design point (ADP). It is then evaluated at various other off-design operating conditions where key performance metrics must be met. An *outer* MDP solver can be used to iterate on cycle input design parameters at the ADP until the required performance metrics are met at all of the off-design flight conditions. Cycle performance itself is evaluated using a separate *inner* cycle (CY) solver that ensures conservation equations (i.e., continuity, energy, and angular momentum) are satisfied at each given flight condition.

The purpose of the ADP is to *size* the engine in terms of mass flow rates and physical flow areas, along with setting the scale factors for the compressor and turbine performance maps. In addition, for the GT-SROR, the rotor diameter and gearbox ratio are calculated based on the design power loading P/D^2 and tip speed ΩR. The setup of the CY solver for the ADP is relatively simple since most of the cycle parameters such as flow rates, rotor power, and compressor pressure ratios are inputs during the design phase. Table 2 shows the design solver terms that appear in the CY solver for

Table 2 Aerodynamic Design Point Solver Setup

Independent Variable	Dependent Condition
HPT PR	N2 Torque Balance
LPT PR	N1 Torque Balance

Table 3 Off-Design Point Solver Setup

Independent Variable	Dependent Condition
Inlet Mass Flow	Nozzle Continuity
Compressor Map Positions	Compressor Continuity
Turbine Pressure Ratios	Turbine Continuity
N1/N2 Shaft Speeds	N1/N2 Torque Balances
Rotor Power	Scheduled C_P or β Target
Fuel Flow	Thrust or Temperature Target

the ADP. Although not shown in Table 2, the ADP solver also sets Mach numbers throughout the engine to hit various compressor and turbine physical sizing targets (such as corrected flow per area). These sizing targets are not specific to the GT-SROR model and do not warrant a detailed discussion.

When the cycle is being evaluated at off-design conditions, the role of the inner cycle solver is to determine the correct operating positions on all of the turbomachinery maps such that component-to-component continuity is maintained, along with varying shaft speeds to maintain a torque balance on the shafts. In addition, the inlet flow area is varied to maintain continuity across the exhaust nozzle. Lastly, the power absorbed by the rotor is set to achieve a scheduled power or thrust coefficient. Additional details on rotor power scheduling are given in Sct. V. Table 3 shows the off-design solver terms that appear in the CY solver for all of the off-design operating points.

The purpose of the outer MDP solver is to vary design point parameters at the ADP so that the engine is sized properly to achieve performance targets under other operating conditions. Table 4 lists the other design points used for the GT-SROR model. Table 5 shows the setup of the MDP solver in order to achieve the desired performance targets. Note that the T41 target refers to the HPT inlet temperature.

V. Power Management Strategy

In a typical turbofan engine, the engine thrust/power (throttle) is set by changing the fuel flow to the engine. The engine power itself is monitored in various ways: fan speed (N1, as a percentage), inter-turbine temperature (ITT) or exhaust gas temperature (EGT), or engine pressure ratio (EPR), which is normally defined as the ratio of turbine exit total pressure to fan inlet total pressure. Although there are different methods to monitor the engine throttle setting, the throttle itself is varied simply by changing fuel flow. However, for an open rotor, with variable pitch blades and vanes, an additional power-setting parameter to the engine is introduced: namely, the power absorbed by the rotor. For a given fan speed, the pitch angle of the rotor blades and vanes can be varied. This leads to a different amount of power absorbed by the rotor, and thus different levels of net thrust. To avoid complicating throttle-setting for the pilot, it is therefore desirable to develop a power management strategy for the engine so that the pilot still only has to control fuel

Table 4 MDP Operating Points

Point	Abbreviation	Purpose
Aerodynamic Design Point	ADP	Engine Sizing
Top-of-Climb	TOC	Thrust Target for Aircraft Rate of Climb
Takeoff	TKO	Maximum Turbine Inlet Temperature
Sea-Level Static	SLS	Thrust Target for Design Aircraft Thrust to Weight

Table 5 MDP Solver Setup

Independent Variable	Dependent Condition
ADP Inlet Mass Flow	ADP to TOC Inlet Corrected Flow Ratio Target
ADP Rotor Power	Rotor Diameter Target
ADP Burner FAR	TOC Thrust Target
TOC Burner FAR	TOC T41 Target
TKO Burner FAR	TKO T41 Target
SLS Burner FAR	SLS Thrust Target
ADP Cooling Flow Fractions	TKO Cooling Flows

flow to the engine in order to set thrust, versus controlling both fuel flow and rotor power simultaneously. In a typical turboprop engine, which has variable pitch propellers, a governor is used to automatically set the propeller pitch angle to maintain a near-constant speed. However, for an architecture with the open rotor on the same shaft as the low-pressure compressor, it is not feasible to run the rotor at a constant speed.

The proposed method is to schedule rotor power as a function of fan speed, which is the typical indicator of engine power, to reduce the number of required inputs from the pilot to set engine thrust. To investigate this, both rotor power and fan speed were varied in the GT-SROR model across combinations of Mach number and altitude that spanned the complete envelope for a typical single-aisle commercial aircraft. Specific fuel consumption (SFC), defined as engine fuel flow (lbm/hr) per pound thrust (lbf), contours were then plotted versus rotor power coefficient and fan speed, as seen in Fig. 9. Based on the contours seen in Fig. 9, it is clear that for a given fan speed, a rotor power coefficient can be found that corresponds to the minimum SFC. The line of C_P values that minimizes SFC across a range of fan speeds is shown in red in Fig. 9. It should be noted that the turbine inlet temperature has an upper limit during off-design operation of the engine, and when this temperature limit is taken into account, the engine is unable to operate at the true minimum SFC point. The dark blue line in Fig. 9 represents the best SFC that can be obtained when the operating T41 limit is taken into account. To better illustrate this, lines of constant T41 were overlaid on top of the SFC contours, as seen in Fig. 10. At the particular operating condition shown (altitude of 30,000 ft and $M_\infty = 0.8$), it can be seen from Fig. 10 that the best operating condition for the engine appears to be maximizing the turbine inlet temperature.

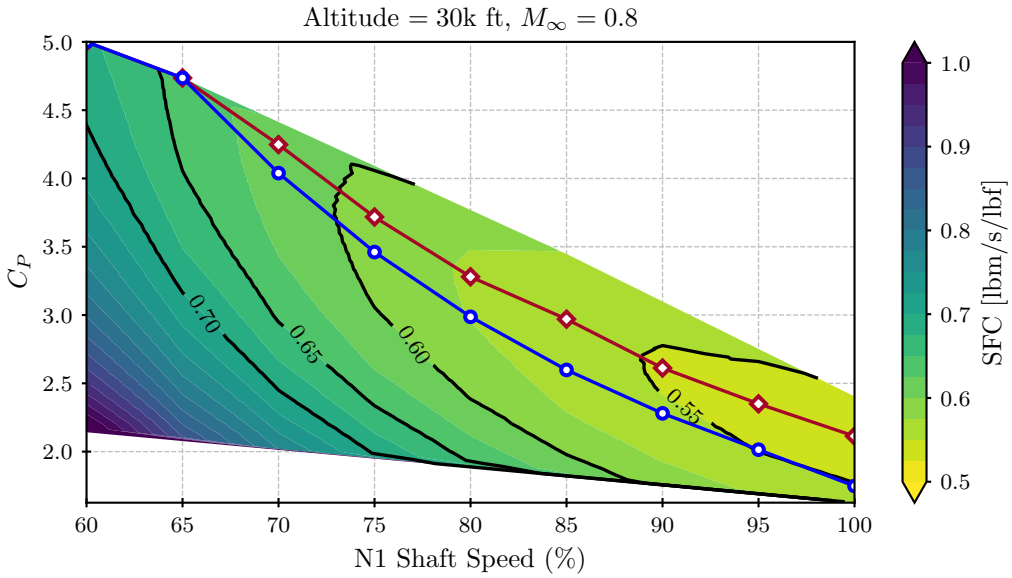

Fig. 9 Contours of engine SFC as a function of C_P and fan speed at 30,000 ft and M_∞ = 0.8. The solid red line represent the minimum SFC for a given fan speed without temperature limits. The solid blue line represents the minimum SFC taking engine temperature limits into account.

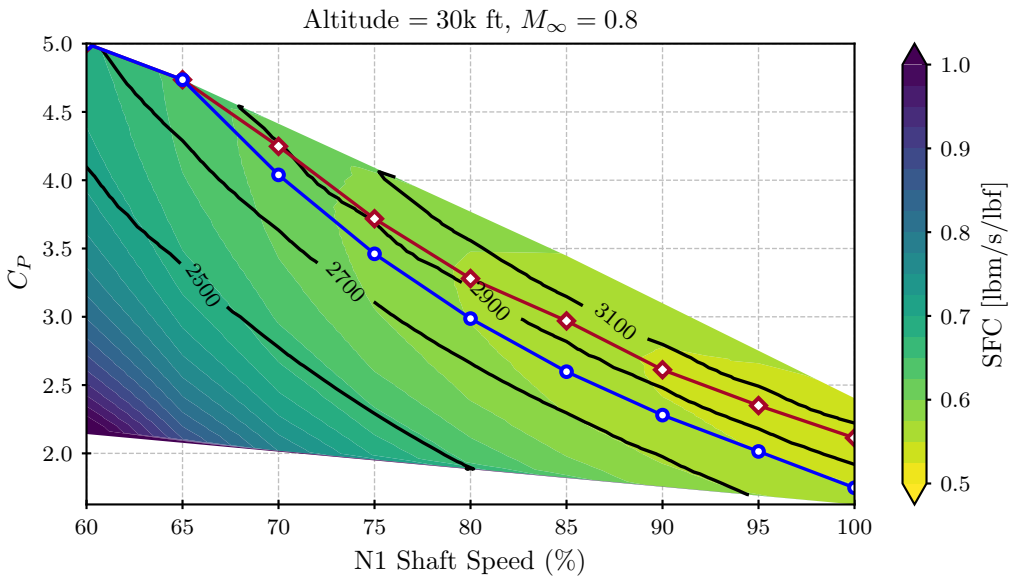

Fig. 10 Lines of constant T41 as a function of C_P and fan speed at 30,000 ft and M_∞ = 0.8. The solid red line represent the minimum SFC for a given fan speed without temperature limits. The solid blue line represents the minimum SFC taking engine temperature limits into account.

The same process can be followed, plotting SFC versus rotor blade pitch angle instead of power coefficient, as seen in Figs. 11 and 12. A comparison of the optimum SFC values in Fig. 9 versus Fig. 11 shows that the optimal SFC follows a much more linear trend when plotted versus rotor pitch angle versus rotor power coefficient.

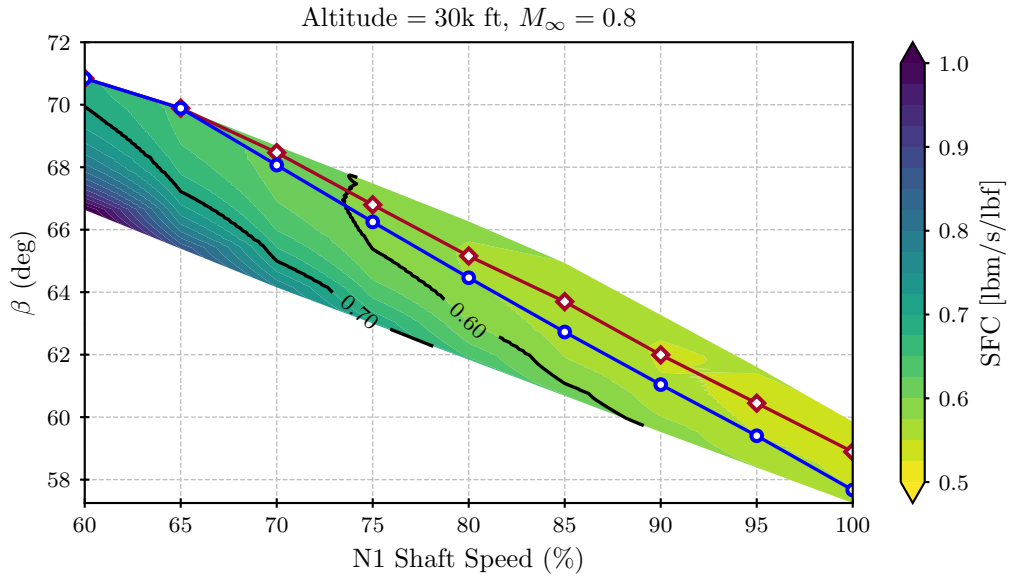

Fig. 11 Contours of engine SFC as a function of β and fan speed at 30,000 ft and M_∞ = 0.8. The solid red line represent the minimum SFC for a given fan speed without temperature limits. The solid blue line represents the minimum SFC taking engine temperature limits into account.

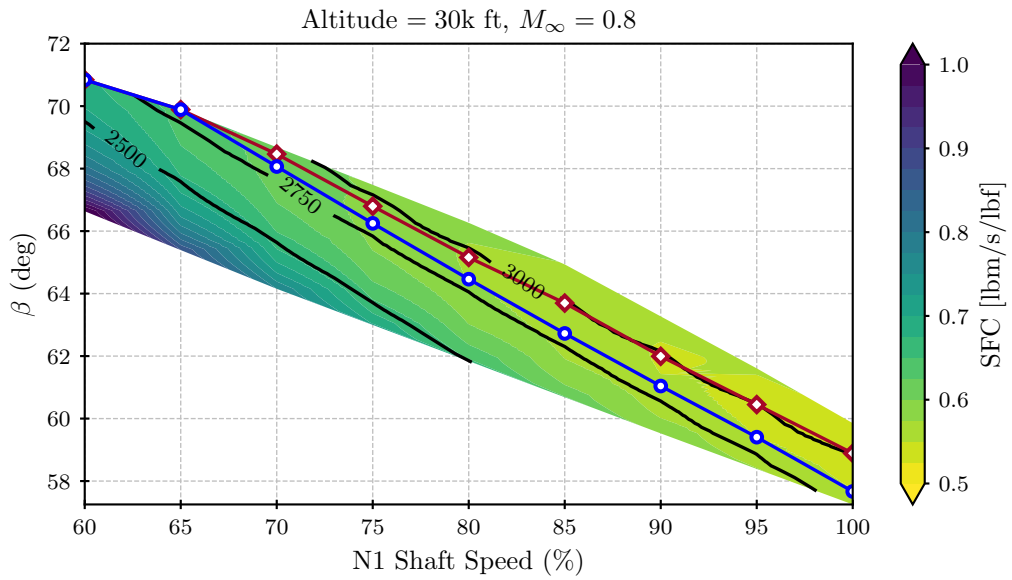

Fig. 12 Lines of constant T41 as a function of β and fan speed at 30,000 ft and M_∞ = 0.8. The solid red line represent the minimum SFC for a given fan speed without temperature limits. The solid blue line represents the minimum SFC taking engine temperature limits into account.

When developing a model of the GE36 unducted fan engine, which operated at a constant speed, Hendricks proposed a linear power management schedule for blade pitch versus Mach number [30]. Fig. 13 shows the optimum blade pitch angle versus M_∞ for 100% N1 and 95% N1, both of which are relatively linear in nature. The similarity between these results and Hendricks' proposed schedule gives some confidence in this method.

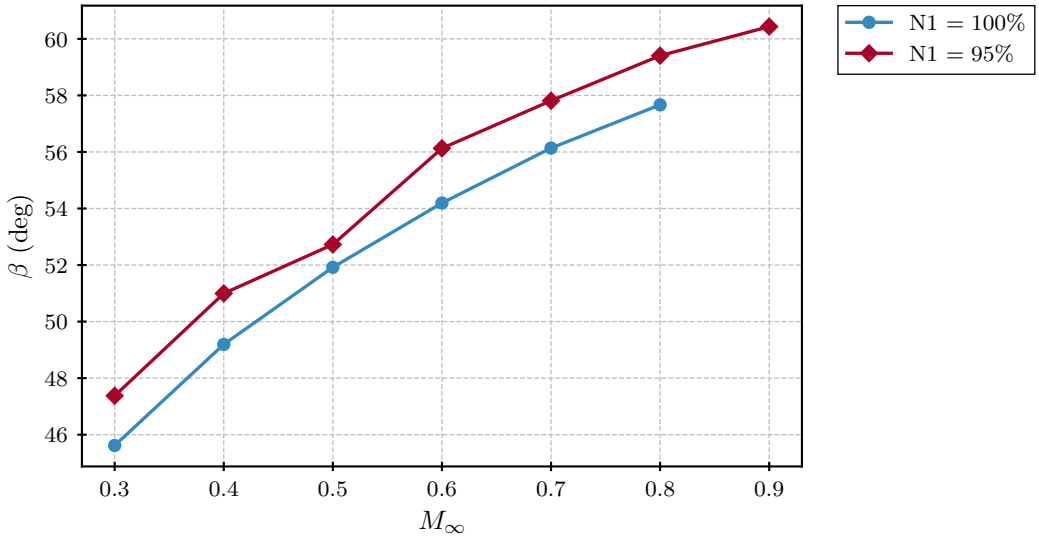

Fig. 13 Optimum Beta versus M_∞ at 100% and 95% N1 Speed

Fig. 14 shows the optimal blade pitch angle lines at Mach = 0.8 for several altitudes. When the engine is allowed to operate at any turbine inlet temperature, the impact of altitude is negligible. This is because rotor performance parameters are normalized with density (see Eq. (1)), and so the atmospheric variation in temperature with altitude is accounted for. However, when the engine is limited by T41, the impact of altitude on the optimal blade pitch angle can

be seen in Fig. 14. The results of determining the optimal power coefficient and blade angle across the entire flight envelope can be seen in Figs. 15 and 16. Note that these are the altitude-averaged minimum SFC lines when ignoring engine temperature limits (so averaging across altitudes is reasonable).

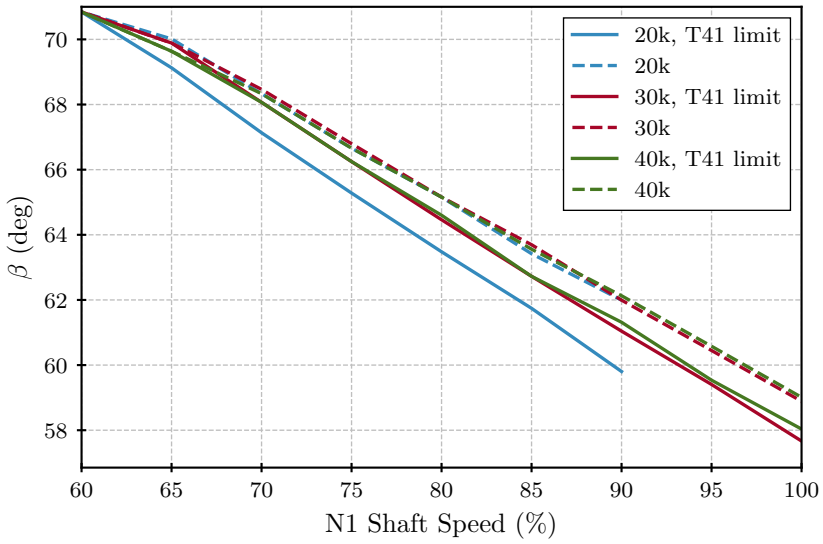

Fig. 14 Optimum Blade Pitch Angle for Minimum SFC versus Fan Speed at M_∞ = 0.8 for various altitudes, with and without engine temperature limits.

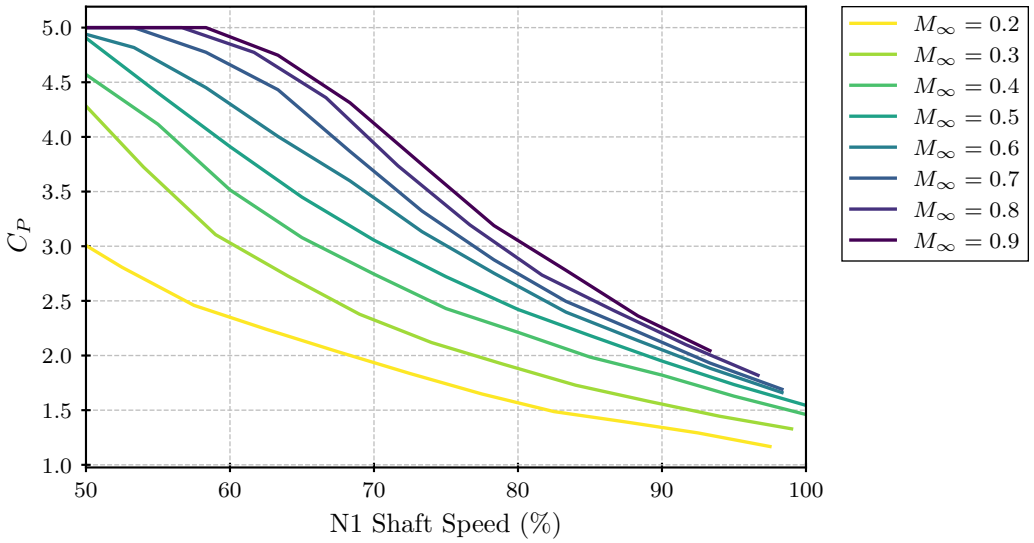

Fig. 15 Optimum Power Coefficient for Minimum SFC versus Fan Speed and Mach Number

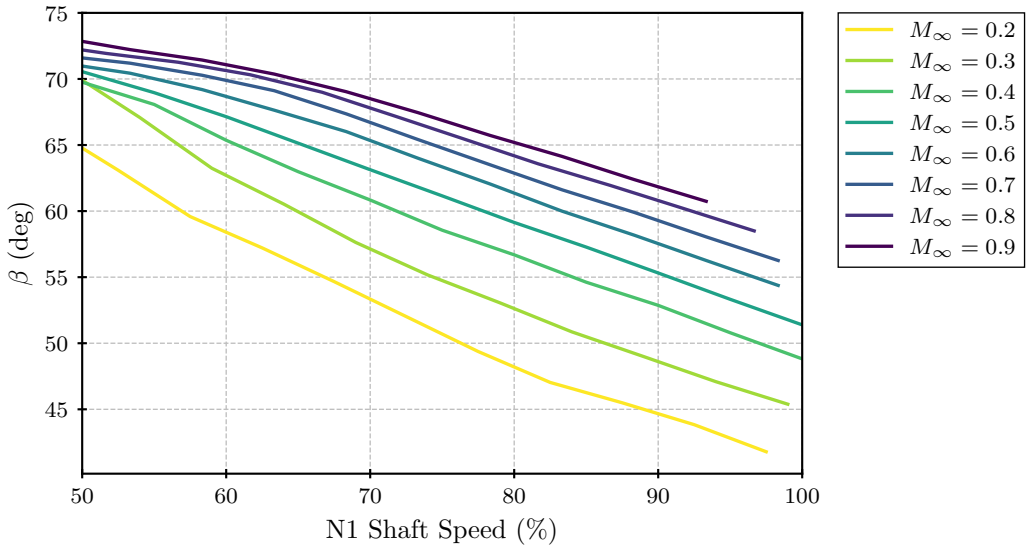

Fig. 16 Optimum Blade Pitch Angle for Minimum SFC versus Fan Speed and Mach Number

Note that both Figs. 15 and 16 do not show static performance (i.e., $M_\infty = 0$). This is primarily due to compressor operability limits for the engine. When generating the engine performance data, compressor stall margin with respect to flow (SMW) was required to remain above 2%. At static conditions, the rotor power had to be set to the maximum power coefficient value within the performance map to avoid violating the compressor stall margin limit. Also note that at low fan speeds and higher Mach numbers, the optimal rotor power coefficient is limited to the highest power coefficient available in the rotor performance map, to avoid extrapolating beyond the rotor map boundaries. This is merely a modeling limitation and should not impact the overall predictions as the aircraft is unlikely to operate at those regimes.

The optimum performance parameter (either blade pitch angle or power coefficient) was tabulated versus fan speed, Mach number, and altitude (to account for the impact of the turbine inlet temperature operating limit) into an NPSS-friendly format so that rotor power could be appropriately scheduled across the flight envelope. While this method is feasible for a single engine design, it is by no means a feasible method when running a design of experiments (DoE) on thousands of different engine designs to determine the best engine cycle. The process of generating the NPSS tables requires evaluating rotor performance at thousands of points across the flight envelope, which would be far too computationally expensive to complete for every single engine design in a large DoE.

To alleviate this computational burden, a different method for determining the optimal rotor performance parameter scheduling is proposed. An examination of the optimum SFC lines in Figs. 16 shows that the relationship between rotor blade pitch angle and fan speed is relatively linear, and monotonic with Mach number for most of the operating N1 speed range. The proposed method is therefore to take advantage of the linear relationship and use a small subset of points within the flight envelope to generate a table lookup to schedule rotor power. Rather than evaluating performance at thousands of operating conditions, performance is evaluated at six different operating conditions, summarized in Table 6. These points were selected because they span the nominal range of operating altitude and Mach number that an aircraft is expected to fly at. The speeds were selected so that they remain within the primarily linear region seen in Fig. 16.

Table 6 Power Management Points

Altitude (ft)	Mach	Target N1 (%)
0	0.25	TKO N1
0	0.25	TKO N1 - 15%
35000	0.5	75%
35000	0.5	95%
35000	0.78	75%
35000	0.78	95%

At each of these six points, the rotor blade angle was swept across a small range of values, and the blade angle that resulted in the minimum engine SFC was tabulated. While generating this table, the turbine inlet temperature limit was automatically enforced, so occasionally the upper fan speed target was not reached. The results of sweeping rotor blade pitch angle across the small subset of points shown in Table 6 are plotted next to the temperature-limited optimal blade angles obtained from the *full* rotor performance envelope exploration in Fig. 17. Examination of Fig. 17 shows that the results of the reduced-envelope closely match the full envelope exploration. The same process was undertaken for the optimum power coefficient, and the results can be seen in Fig. 17. The non-linear nature of the optimum power coefficient is quite apparent in Fig. 17. It is important to note that NPSS was set to perform linear interpolation and extrapolation when using these tables to set rotor power.

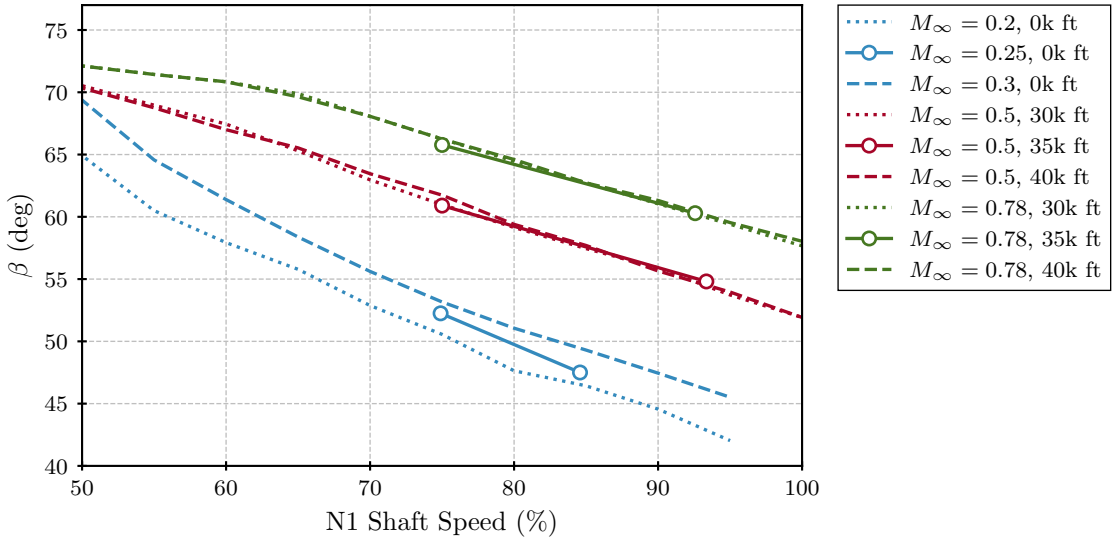

Fig. 17 Reduced-Design Space Optimum Blade Pitch Angle Comparison

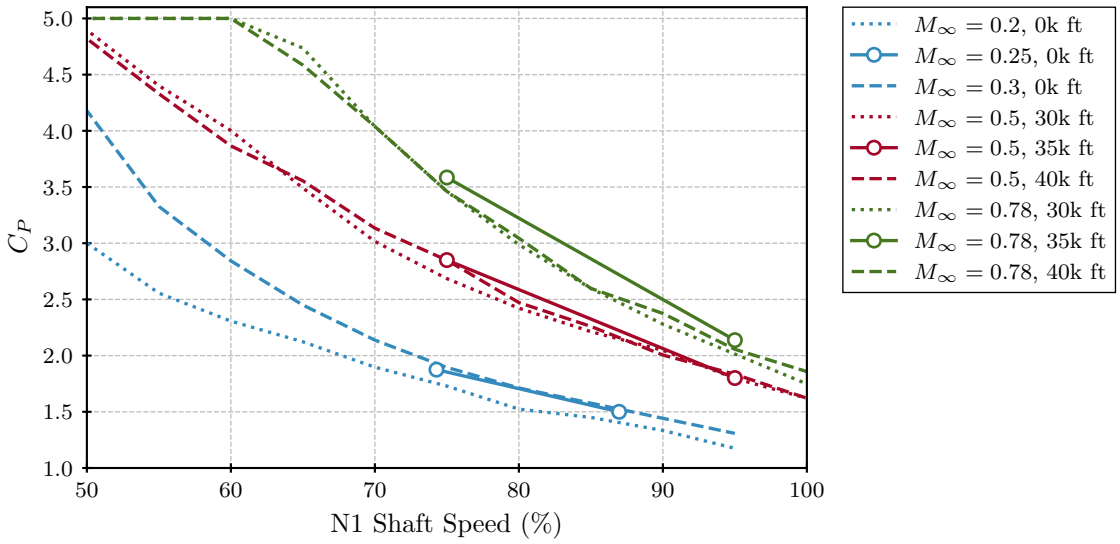

Fig. 18 Reduced-Design Space Optimum Power Coefficient Comparison

VI. Aircraft Performance Evaluation

To evaluate the effectiveness of the reduced-design space rotor power scheduling versus the full design space scheduling, a method is needed to evaluate engine performance for the four different proposed power scheduling techniques. NASA's Flight Optimization system (FLOPS) was used to evaluate engine performance in the context of a 150 passenger aircraft flying a design mission of 3402 nautical miles. The aircraft takeoff thrust to weight ratio was set at 0.2811, while the takeoff wing loading was set at 128.33 lb/ft^2. To evaluate each method of rotor scheduling, a design loop was developed that is capable of generating an engine design and then evaluating that engine's performance for the specified aircraft mission. This design loop can be seen in Fig. 19, and is closely modeled after the design process of the Environmental Design Space (EDS) described by Kirby and Mavris [33].

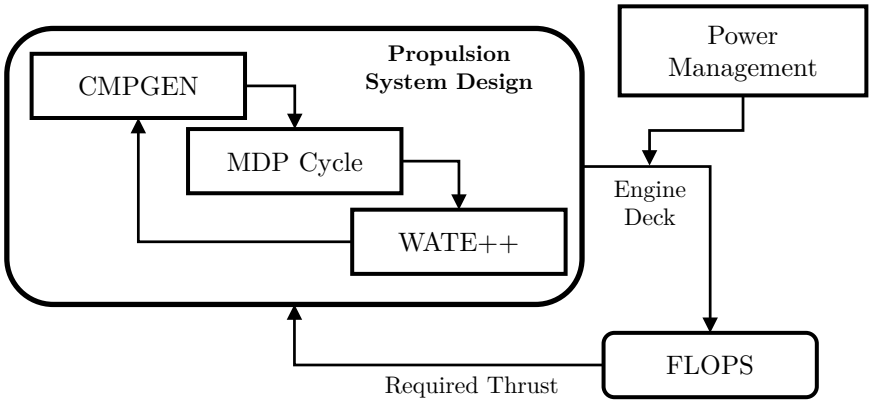

Fig. 19 Propulsion System / Aircraft Design Loop

In the propulsion system design loop, NASA's CMPGEN software is first used to generate compressor performance maps for each compressor in the engine [32]. The engine cycle is then designed using the MDP process, and the results of this cycle are fed into NASA's WATE++ program, which is a weight estimation tool for propulsion systems [34, 35]. The results of WATE++ are fed back into CMPGEN, and the propulsion system design loop runs until there is no significant change in the WATE++ results. Once the propulsion system design loop is converged, an engine performance deck is generated by running the engine in off-design mode at various power settings across the flight envelope. The

engine fuel flow and open rotor power which govern off-design performance are determined by the power management strategy. This performance deck is then loaded into FLOPS, which *flies* the aircraft and evaluates the total fuel burn for the design mission [36]. If the sea-level static thrust in the engine performance deck does not match the calculated takeoff weight multiplied by the takeoff thrust to weight ratio, FLOPS automatically *scales* the engine deck. Since fuel burn does not scale directly with thrust, a new sea level static thrust target is sent back to the propulsion system design loop, and the whole process iterates until FLOPS no longer attempts to scale the engine deck. Using this design loop, it is then possible to directly compare the overall mission-level results of the four different power management strategies proposed for the open rotor engine.

VII. Results

The design loop described in Section VI was used to evaluate the four different power management strategies shown in Table 7. Cases 1 and 3 use tables of rotor pitch angle and power coefficient, respectively, which were tabulated versus fan speed, Mach number, and altitude. These tables were generated using the full sweep of the rotor performance envelope, which involved comparing the SFC for thousands of combinations of operating points. Cases 2 and 4 use the reduced rotor envelope, where the optimum value of pitch angle or power coefficient was found at only six points in the overall rotor performance envelope.

Table 7 Design Cases

Case	Control Parameter	Schedule Source
1	β	Full Envelope Evaluation
2	β	Six-Point Table
3	C_P	Full Envelope Evaluation
4	C_P	Six-Point Table

Some salient performance results of executing the design loop shown in Fig. 19 for each power management strategy are summarized in Table 8. Cases 1 and 3 yield aircraft designs that are nearly identical, with mission block fuel coming out to within 1%. This is expected, since both methods used the same underlying data for the rotor power scheduling, differentiated only by the actual rotor performance parameter used in the schedule (blade pitch angle versus power coefficient). Case 2, the six-point pitch angle schedule, actually yields the best overall performance, although the difference between Cases 2 and 3 is essentially negligible. Case 4, the six-point power coefficient schedule, however, yields results that are significantly worse, with mission fuel burn over 7% worse than the six-point pitch angle schedule. Looking back at Fig. 18, this result is not particularly surprising. The simple six-point schedule does not appropriately capture the non-linear nature of the optimum power coefficient. Therefore, when using this schedule, the engine operates further away from the optimum SFC power setting and thus experiences higher fuel consumption, leading to the larger mission fuel weight and larger overall aircraft design.

Table 8 Aircraft Performance Result Comparison

Case	Mission Fuel (lbm)	Gross Weight (lbm)	S_{ref} (ft^2)	SLS Thrust (lbf)[a]
1	27303	153267	1195	21542
2	26948	152687	1191	21460
3	27045	153085	1194	21516
4	28888	155308	1211	21829

[a] per engine

The results shown in Table 8 indicate that rotor power can be scheduled using either the full-envelope schedules or using the six-point schedule with rotor blade pitch angle as the control parameter, with negligible difference in overall aircraft mission performance. However, the aircraft performance results do not tell the whole story. Table 9 shows the computational side of the story and contains execution time, along with the the overall number of solver iterations for the two primary solvers within the NPSS model for each design case. Recall from Fig. 19 that the model contains a

Cycle solver nested within the multiple design point solver, both of which iterate with FLOPS. A majority of execution time for the design loop is spent by the Cycle solver generating the engine performance decks that are fed into FLOPS. This involves a large number of iterations of the Cycle solver, since several hundred combinations of altitude, Mach number, and power setting are required to build a complete engine deck. Examination of the results in Table 9 show that Case 2, the six-point pitch angle schedule, is clearly the best-performing method from a computational standpoint. Computational efficiency is desired since optimizing the propulsion system typically involves investigating thousands of potential engine designs. The six-point schedule is able to run nearly three times faster than the pitch angle schedule built from the full envelope rotor evaluation. Cases 3 and 4, the rotor power coefficient schedules, were significantly slower.

Table 9 Design Loop Computational Comparison

Case	Execution Time (min:sec)	MDP Solver Iterations	Cycle Solver Iterations
1	11:00	526	219023
2	3:50	527	65444
3	24:37	525	499169
4	27:08	749	581687

The slower execution time and higher cycle solver iteration counts for 1, 3, and 4 are due to non-convergence issues that were observed during the engine deck generation phase. Specifically, for cases 3 and 4, recall that the equation for rotor power coefficient, Eq. (1), shows that the power coefficient is a function of rotor speed cubed. In this open rotor architecture, the rotor is directly linked via a reduction gearbox to the low-speed shaft, N1. Since rotor power was scheduled versus N1, it is believed that this cubic dependence on speed leads to very steep gradients as the solver builds the Jacobian matrix to find a converged solution. These steep gradients are then likely to cause the solver to flutter without finding a converged solution within the specified solver iteration limit for each point in the engine deck. Case 1, which uses the full-envelope schedule for blade pitch angle also experienced quite a few solver non-convergence issues throughout the envelope, although at a significantly lower rate than Cases 3 or 4. Case 2 experienced almost no convergence issues when generating the engine deck, which explains the significantly faster execution time and lower overall cycle solver iteration count.

It should also be noted that the overall execution time and solver counts for Cases 1 and 3 in Table 9 do not account for the extra time required to sweep rotor power across the entire flight envelope in order to build the complete altitude-dependent rotor pitch angle and power coefficient schedules. The six-point method, however, was built directly into the design loop shown in Fig. 19, so the computational cost is accounted for in Table 9.

VIII. Conclusion

The aerospace industry continues to search for way to improve fuel burn as a means to reduce harmful emissions and lower the overall carbon footprint aircraft. As shown here, one such way is the introduction of new propulsion system architectures intended to drastically improve propulsive efficiency, such as open rotor (or unducted fan) architectures.

This paper presented the methods used to develop an open rotor propulsion system architecture, similar to the proposed CFM RISE architecture. A Blade Element Momentum Theory (BEMT) method was used to generate open rotor performance maps, which were used in the Numerical Propulsion System Simulation (NPSS) performance model of the overall propulsion system. Furthermore, a power management strategy was developed that could be easily integrated into an overall propulsion system and aircraft design loop.

One drawback to the open rotor architecture is the presence of an additional power-setting parameter for the engine. A traditional turbofan engine only varies fuel flow in order to set the power. However, the rotor blades in the Open Rotor configuration have a variable pitch, which allows the rotor to absorb different levels of power from the engine core for a given shaft speed. This introduces an undesirable extra level of complexity, since pilots will not want to have to try and vary fuel flow and rotor power at the same time. In a turboprop, which also has variable pitch blades, the blade pitch is varied by a governor in order to maintain a relatively constant rotational speed. For the open rotor architecture investigated, however, the rotor is on the same shaft as the low-pressure compressor and low-pressure turbine, so fixing the shaft speed would be an untenable solution. Therefore, a method is needed to schedule rotor power throughout the flight envelope so that the pilot is able to use only fuel flow when setting overall engine power.

It was shown that for a given engine cycle, the off-design performance could be evaluated for a large number of combinations of rotor power and N1 shaft speed, and look-up tables could be generated in order to schedule the optimum rotor power versus altitude, Mach number, and N1 speed that would minimize engine SFC. This process, unfortunately, is computationally expensive, and resulted in off-design performance that experienced a large number of solver non-convergence issues.

However, a method was developed to generate a schedule of rotor blade pitch angle versus Mach number and N1 shaft speed using only six points from the flight envelope. This method was able to produce nearly identical aircraft-level mission fuel burn when compared to the schedules based on the full envelope evaluation of rotor performance, but with a significant reduction in computational time required to evaluate the combined propulsion and aircraft system. It was also shown that scheduling rotor power using the rotor blade pitch angle led to significant computational improvements versus using schedules based on the rotor power coefficient, due to the more linear relationship between pitch angle and shaft speed.

One key area identified for future work would be to explore an architecture where the open rotor is on a separate shaft with a free-power turbine, similar to typical turboshaft engines. Such an architecture would allow for greater control over the rotor rotational speed. Furthermore, this work was focused primarily on developing an efficient power management strategy. With a robust power management strategy in place, a logical next step is to attempt to find the rotor design parameters and cycle design parameters that minimize overall mission fuel burn.

Acknowledgments

Robert Clark was supported in this research by the Department of Defense (DoD) through the National Defense Science and Engineering Graduate (NDSEG) Fellowship Program.

References

[1] Khalid, S. A., Wojno, J. P., Breeze-Stringfellow, A., Lurie, D. P., Wood, T. H., Ramakrishnan, K., and Paliath, U., "Open rotor designs for low noise and high efficiency," *Proceedings of the ASME Turbo Expo*, Vol. V06CT39A00, 2013, pp. 1–14. https://doi.org/10.1115/GT2013-94736.

[2] Van Zante, D. E., "Progress in Open Rotor Research: A U.S. Perspective," *Volume 1: Aircraft Engine; Fans and Blowers; Marine*, American Society of Mechanical Engineers, 2015, pp. 1–14. https://doi.org/10.1115/GT2015-42203.

[3] Dorsey, A., and Uranga, A., "Design Space Exploration of Future Open Rotor Configurations," *AIAA Propulsion and Energy 2020 Forum*, American Institute of Aeronautics and Astronautics, Reston, Virginia, 2020, pp. 1–30. https://doi.org/10.2514/6.2020-3680.

[4] Groeneweg, J. F., and Bober, L. J., "NASA Advanced Propeller Research," NASA-TM-101361, 1988.

[5] Li, Q., Öztürk, K., Sinnige, T., Ragni, D., Eitelberg, G., Veldhuis, L., and Wang, Y., "Design and experimental validation of swirl-recovery vanes for propeller propulsion systems," *AIAA Journal*, Vol. 56, No. 12, 2018, pp. 4719–4729. https://doi.org/10.2514/1.J057113.

[6] "Full Scale Technology Demonstration Of A Modern CounterRotating Unducted Fan Engine Concept: Design Report," NASA-CR-180867, December 1987.

[7] "Full Scale Technology Demonstration Of A Modern CounterRotating Unducted Fan Engine Concept: Engine Test," NASA-CR-180869, December 1987.

[8] Hager, R. D., and Vrabel, D., "Advanced Turboprop Project," NASA-SP-495, January 1988.

[9] Brouckaert, J.-F., Mirville, F., Phuah, K., and Taferner, P., "Clean Sky research and demonstration programmes for next-generation aircraft engines," *The Aeronautical Journal*, Vol. 122, No. 1254, 2018, pp. 1163–1175. https://doi.org/10.1017/aer.2018.37.

[10] Barbosa, F. C., "Open Rotor Engine Technology Review – A Tool for Efficiency," *SAE Technical Papers*, 2021. https://doi.org/10.4271/2020-36-0108.

[11] CFM, "CFM RISE Program," CFM RISE Whitepaper, July 2021.

[12] Zatorski, Darek Tomasz and Hamel, Jeffrey and Breeze-Stringfellow, Andrew, "Unducted Thrust Producing System Architecture," U. S. Patent 10,704,410, July 7 2020.

[13] Larrabee, E. E., and French, S. E., "Minimum Induced Loss Windmills and Propellers," *Wind Engineering 1983*, Vol. 15, Elsevier, 1984, pp. 317–327. https://doi.org/10.1016/B978-0-444-42342-9.50042-3.

[14] Larrabee, E. E., "Five Years Experience with Minimum Induced Loss Propellers - Part I: Theory," *SAE Technical Papers*, Vol. 93, 1984, pp. 1130–1137. https://doi.org/10.4271/840026.

[15] Drela, M., "QPROP formulation," published online, June 2006. Available: http://web.mit.edu/drela/Public/web/qprop/.

[16] Virtanen, P., Gommers, R., Oliphant, T. E., Haberland, M., Reddy, T., Cournapeau, D., Burovski, E., Peterson, P., Weckesser, W., Bright, J., van der Walt, S. J., Brett, M., Wilson, J., Millman, K. J., Mayorov, N., Nelson, A. R. J., Jones, E., Kern, R., Larson, E., Carey, C. J., Polat, İ., Feng, Y., Moore, E. W., VanderPlas, J., Laxalde, D., Perktold, J., Cimrman, R., Henriksen, I., Quintero, E. A., Harris, C. R., Archibald, A. M., Ribeiro, A. H., Pedregosa, F., van Mulbregt, P., and SciPy 1.0 Contributors, "SciPy 1.0: Fundamental Algorithms for Scientific Computing in Python," *Nature Methods*, Vol. 17, 2020, pp. 261–272. https://doi.org/10.1038/s41592-019-0686-2.

[17] Goldstein, S., "On the vortex theory of screw propellers," *Proceedings of the Royal Society of London. Series A, Containing Papers of a Mathematical and Physical Character*, Vol. 123, No. 792, 1929, pp. 440–465. https://doi.org/10.1098/rspa.1929.0078.

[18] Rohrbach, C., Metzger, F. B., Black, D. M., and Ladden, R. M., "Evaluation of wind tunnel performance testings of an advanced 45 deg swept 8-bladed propeller at Mach numbers from 0.45 to 0.85," NASA-CR-3505, March 1982.

[19] Stefko, G., and Jeracki, R., "Wind tunnel results of advanced high speed propellers in the takeoff, climb, and landing operating regimes," *21st Joint Propulsion Conference*, American Institute of Aeronautics and Astronautics, 1985. https://doi.org/10.2514/6.1985-1259.

[20] Chandrasekaran, B., and Bartlett, G., "Method for Calculating Effects of a Profan on Aircraft Aerodynamics At Subsonic Speeds." *19th Joint Propulsion Conference*, American Institute of Aeronautics and Astronautics, 1983. https://doi.org/10.2514/6.1983-1216.

[21] Veldhuis, L., "Propeller Wing Aerodynamic Interference," Doctoral thesis, Delft University of Technology, June 2005.

[22] Playle, S. C., Korkan, K. D., and Von lavante, E., "A numerical method for the design and analysis of counter-rotating propellers," *Journal of Propulsion and Power*, Vol. 2, No. 1, 1986, pp. 57–63. https://doi.org/10.2514/3.22845.

[23] Smith, D. A., "Aerodynamic and Aeroacoustic Analysis of Counter Rotating Open Rotors," Ph.D. Thesis, University of Manchester, 2020. https://doi.org/10.13140/RG.2.2.23515.59682.

[24] Mastropierro, F. S., Sebastiampillai, J., Jacob, F., and Rolt, A., "Modeling Geared Turbofan and Open Rotor Engine Performance for Year-2050 Long-Range and Short-Range Aircraft," *Journal of Engineering for Gas Turbines and Power*, Vol. 142, No. 4, 2020, pp. 1–12. https://doi.org/10.1115/1.4045077.

[25] Jones, S. M., "An Introduction to Thermodynamic Performance Analysis of Aircraft Gas Turbine Engine Cycles Using the Numerical Propulsion System Simulation Code," NASA TM-2007-214690, March 2007.

[26] Schutte, J., "Simultaneous multi-design point approach to gas turbine on-design cycle analysis for aircraft engines," Ph.D. Dissertation, Georgia Institute of Technology, April 2009.

[27] Schutte, J., Tai, J., and Mavris, D., "Multi Design Point Cycle Design Incorporation into the Environmental Design Space," *48th AIAA/ASME/SAE/ASEE Joint Propulsion Conference & Exhibit*, American Institute of Aeronautics and Astronautics, 2012. https://doi.org/10.2514/6.2012-3812.

[28] Schutte, J., Tai, J., Sands, J., and Mavris, D., "Cycle Design Exploration Using Multi-Design Point Approach," *Turbo Expo: Power for Land, Sea, and Air, Volume 1: Aircraft Engine; Ceramics; Coal, Biomass and Alternative Fuels; Controls, Diagnostics and Instrumentation*, American Society of Mechanical Engineers, 2012, pp. 271–281. https://doi.org/10.1115/gt2012-69334.

[29] "AS755F: Aircraft Propulsion System Performance Station Designation," *SAE International*, 2014.

[30] Hendricks, E. S., "Development of an Open Rotor Cycle Model in NPSS Using a Multi-Design Point Approach," NASA TM-2011-217225, January 2011.

[31] Bellocq, P., Sethi, V., Cerasi, L., Ahlefelder, S., Singh, R., and Tantot, N., "Advanced Open Rotor Performance Modelling for Multidisciplinary Optimization Assessments," *Turbo Expo: Power for Land, Sea, and Air, Volume 1: Aircraft Engine; Ceramics; Coal, Biomass and Alternative Fuels; Education; Electric Power; Manufacturing Materials and Metallurgy*, 2010, pp. 287–302. https://doi.org/10.1115/GT2010-22963, URL https://doi.org/10.1115/GT2010-22963.

[32] Converse, G., and Giffin, R., "Extended Parametric Representation of Compressor Fans and Turbines, Volume I - CMGEN User's Manual," NASA-CR-174645, March 1984.

[33] Kirby, M. R., and Mavris, D. N., "The environmental design space," *ICAS Secretariat - 26th Congress of International Council of the Aeronautical Sciences 2008, ICAS 2008*, Vol. 1, 2008, pp. 3581–3589.

[34] G.W. Onat, K., E., "A Method to Estimate Weight and Dimensions of Large and Small Gas Turbine Engines," *NASA-CR-159481*, 1979, pp. 1–133.

[35] Tong, M. T., Halliwell, I., and Ghosn, L. J., "A computer code for gas turbine engine weight and disk life estimation," *Journal of Engineering for Gas Turbines and Power*, Vol. 126, 2004, pp. 265–270. https://doi.org/10.1115/1.1691980.

[36] McCullers, L., "Flight Optimization System, Release 8.11, User's Guide," 2009.